

Rotation periods of late-type dwarf stars from time-series high-resolution spectroscopy of chromospheric indicators

A. Suárez Mascareño^{1,2} ^{*}, R. Rebolo^{1,2,3}, J. I. González Hernández^{1,2}, M. Esposito^{1,2}

¹ *Instituto de Astrofísica de Canarias, E-38205 La Laguna, Tenerife, Spain*

² *Universidad de La Laguna, Dpto. Astrofísica, E-38206 La Laguna, Tenerife, Spain*

³ *Consejo Superior de Investigaciones Científicas, Spain*

Written - 2015

ABSTRACT

We determine rotation periods of a sample of 48 late F-type to mid-M dwarf stars using time-series high-resolution spectroscopy of the Ca II H&K and H α chromospheric activity indicators. We find good agreement between the rotation periods obtained from each of these two indicators. An empirical relationship between the level of chromospheric emission measured by $\log_{10}(R'_{\text{HK}})$ and the spectroscopic rotation periods is reported. This relation is largely independent of the spectral type and the metallicity of the stars and can be used to make a reliable prediction of rotation periods for late K to mid-M dwarfs with low levels of activity. For some stars in the sample, the measured spectroscopic rotation periods coincide, or are very close, to the orbital periods of postulated planets. In such cases, further studies are needed to clarify whether the associated periodic radial velocity signals reveal the existence of planets or are due to magnetic activity.

Key words: Stars: activity — Stars: chromospheres — Stars: rotation — starspots — planetary systems

1 INTRODUCTION

Magnetic activity influences spectral lines (Dravins 1985) and produces inhomogeneities in the stellar surface, which, combined with rotation, causes Doppler shifts of the stellar spectrum (Saar & Donahue 1997). Changes in the distribution of spots induce apparent Doppler shifts from less than one to dozens of metres per second, depending on the level of stellar activity (Huélamo et al. 2008; Pont, Aigrain & Zucker 2011; Hatzes 2013). When these induced signals are periodic, they could be mistaken for planetary signals. In fact, stellar activity is one of the most important causes of false alarm signals in the analysis of high precision RV time series. Disentangling these signals from a real planetary signal in RV curves is a crucial issue when searching for terrestrial exoplanets. Since the exoplanet community started to search for small planets there has always been a concern that the intrinsic variability of the stellar surface (Baliunas et al. 1997) could render impossible the detection of the low amplitude radial velocity (RV) signals caused by terrestrial planets (Queloz et al. 2001; Dumusque et al. 2012; Santos et al. 2014). The precise determination of the rotation pe-

riods of stars is a crucial first step in discriminating true planetary signals from those induced by the stellar activity.

A well-known connection between stellar activity and rotation has been widely used to estimate rotation periods through stellar models (Skumanich 1972; Catalano & Marilli 1983; Baliunas et al. 1983). Rotation periods have usually been measured from periodic variations in the stellar luminosity associated with the distribution of superficial magnetic spots. These surface structures are sufficiently stable in time to span longer than the rotation period of the star (Robertson et al. 2015) and to make possible the measurement of stellar rotation periods from extensive photometry time series (Messina & Guinan 2002; Kiraga & Stepień 2007). However, these photometric variations are not always strong enough to be detected in stars of very low activity where many RV searches have been performed.

Stellar induced radial velocity variations come mainly from two different sources. First, stellar spots are cooler and radiate less than other regions of the stellar photosphere, thus affecting the photospheric line profiles and therefore the RV measurements. This effect changes as the star rotates. Then stellar magnetic activity creates regions in which the convective currents are altered, thereby changing the ingoing or outgoing flux of material in parts of the star's surface

^{*} E-mail: asm@iac.es

(Dumusque, Boisse & Santos 2014). The position and distribution of these spots and magnetically active regions is strongly dependent on the long term magnetic cycle of the star, so it usually extends over more than a few rotational periods. The second effect produces an apparent change in the radial velocity of the star that becomes more important in later stellar types (Robertson et al. 2014), but it also results in a change in the intensity of the chromospheric emission lines. Since we integrate the whole light of the visible side of the star, the observed fluxes of the lines change with stellar rotation. Measuring these flux variations in spectroscopic time series of chromospheric lines can therefore reveal the rotation period of a star (Dravins, Lindegren & Nordlund 1981; Dravins 1982; Livingston 1982; Brandt & Solanki 1990; Donahue, Saar & Baliunas 1996; Lindegren & Dravins 2003; Meunier, Desort & Lagrange 2010; Lovis et al. 2011; Howard et al. 2014). This has been possible even for stars of very low activity (Dumusque et al. 2012; Robertson et al. 2014). In this paper we use high quality spectroscopic time series of low-activity late-type dwarfs to investigate the time variability of chromospheric indicators and determine rotation periods.

2 STELLAR SAMPLE AND SPECTROSCOPIC DATA

Our sample consists of 48 main-sequence stars from the solar vicinity, covering from late F-type to mid M-type stars, with apparent magnitudes m_V in the range 4–13. The selected stars come from planet-hunting programs using HARPS (Mayor et al. 2003) and therefore have a bias towards low chromospheric activity ($\log_{10}(R'_{HK}) < -4.5$). We search in the HARPS ESO public data archive for stars with spectra available in more than 20 individual observing nights as for April 2014. The sampling should be appropriate for the detection of periodic signals compatible with the rotation of low activity stars. In total, more than 6400 spectra have been analysed in this work. In Table 5 we provide information on the number of spectra, time baseline, and several properties of the stars of our sample.

HARPS is a fibre-fed high resolution echelle spectrograph installed at the 3.6 m ESO telescope in La Silla Observatory (Chile). The instrument has a resolving power $R \sim 115\,000$ over a spectral range from 378 to 691 nm and has been designed to attain very high long-term radial velocity accuracy. It is contained in a vacuum vessel to avoid spectral drifts due to temperature and air pressure variations, thus ensuring its stability. HARPS is equipped with its own pipeline providing extracted and wavelength-calibrated spectra, as well as RV measurements and other data products such as cross-correlation functions and their bisector profiles.

For our analysis we use the extracted order-by-order wavelength-calibrated spectra produced by the HARPS pipeline. For a given star, the change in atmospheric transparency from day to day causes variations in the flux distribution of the recorded spectra that are particularly relevant in the blue where we intend to measure Ca II lines. In order to minimize the effects related to these atmospheric changes we create a spectral template for each star by de-blazing and co-adding every available spectrum and use the co-added

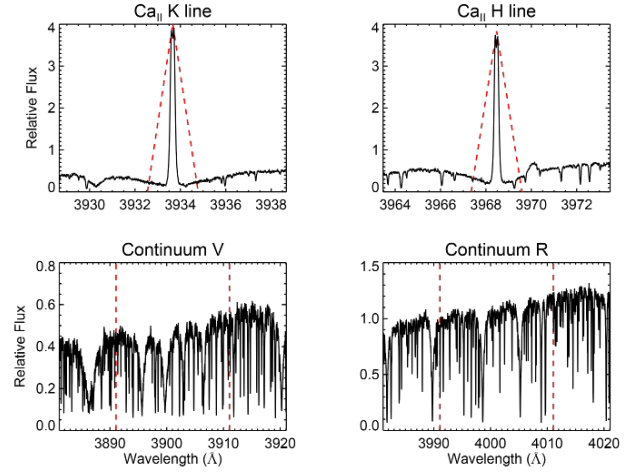


Figure 1. CA II H&K filter of the spectrum of star GJ176, with the same shape as the Mount Wilson Ca II H&K passband.

spectrum to correct the order-by-order fluxes of the individual ones. We also correct each spectrum for the Earth's barycentric radial velocity and the radial velocity of the star using the measurements given by the standard pipeline and re-binned the spectra into a wavelength-constant step. Using this HARPS dataset, we expect to have high quality spectroscopic indicators to monitor tiny stellar activity variations with high accuracy.

3 ACTIVITY INDICATORS

3.1 The HARPS Ca II H&K Index

Following the original Mount Wilson Observatory procedure to characterize stellar activity, we define the same spectral passband as used in the original Mount Wilson HKP-2 spectrophotometer (Vaughan et al. 1981) and compute the HARPS S-index. For the CA II H&K line cores, we define two triangular-shaped passbands with an FWHM of 1.09 Å centred at 3968.470 Å and 3933.664 Å respectively. For the continuum bands we define two 20 Å wide bands centred at 3901.070 Å (V) and 4001.070 Å (R). Figure 1 shows the shape of the filters.

Then the S-index is defined as:

$$S = \alpha \frac{N_H + N_K}{N_R + N_V}, \quad (1)$$

where N_H, N_K, N_R and N_V represent the total flux in each passband, while α is a calibration constant usually fixed at the value of 2.3. As explained in Lovis et al. (2011), the Mount Wilson spectrophotometer is designed so that the H & K bands get 8 times as much flux as in a normal spectrograph, so in order to be at the same scale we fixed the calibration constant as 2.3 times 8.

The S index gives the Ca II H&K core flux normalized to the neighbouring continuum. We use this index to study periodicities related to the rotation of the star. This index contains both photospheric and chromospheric contributions. This does not have any impact when analysing one star, but to be able to compare different stars we have

to subtract the photospheric contribution and normalize the chromospheric flux to the bolometric luminosity of the star. Following Noyes et al. (1984), we compute the R'_{HK} , which is defined as:

$$R'_{\text{HK}} = 1.34 \cdot 10^{-4} \cdot C_{\text{cf}}(B - V) \cdot S - R_{\text{phot}}(B - V), \quad (2)$$

where $C_{\text{cf}}(B - V)$ is the conversion factor that corrects flux variations in the continuum passbands and normalizes to the bolometric luminosity. The Noyes et al. (1984) original bolometric correction is based on the Middelkoop (1982) calibration, which is still widely used nowadays. But this calibration is only reliable in a narrow colour range (from $B - V \sim 0.45$ to ~ 1.2). Our sample also contains stars outside that range. This bolometric correction has been extended at least once (Rutten 1984), but our sample still exceeds the range of application of the updated calibration. In our case, we can directly measure the bolometric correction from the spectra. To do so we followed the original Middelkoop (1982) and Rutten (1984) procedure. The factor C_{cf} is defined as as:

$$C_{\text{cf}} = (S_R + S_V) \cdot 10^{-4} \cdot 10^{0.4(m_v + BC)}, \quad (3)$$

where S_R and S_V are the mean fluxes measured in the continuum passbands, m_v is the visual magnitude in the V band and BC is the bolometric correction according to Johnson (1966). Figure 2 shows how our measured values of the bolometric correction compare to the $B - V$ colour of the stars. We included the measurements from Rutten (1984) for comparison.

For our stars we are using the measured bolometric correction to the index instead of the calibration, but for the future we have decided to provide a new calibration based on our own measurements and those by Rutten (1984). Fitting a third-order least-squares polynomial to the data, we obtain the following correction factor, which is valid in the range from $B - V \sim 0.4$ to $B - V \sim 1.9$.

$$\log_{10} C_{\text{cf}} = 0.668(B - V)^3 - 1.270(B - V)^2 - 0.645(B - V) - 0.443. \quad (4)$$

Figure 1 shows the shape of the H & K bands, they are wide enough to ensure that we do not miss light from the core emission line. But this also allows some photospheric contribution to the measured flux in the wings of the band. Let us call the photospheric contribution to the H & K passbands R_{phot} . This contribution was modelled by Hartmann et al. (1984), who gives a useful relation for the cases where there is no direct access to spectroscopic data, but in our case we can measure this parameter. The R_{phot} is just:

$$R_{\text{phot}} = 1.34 \cdot 10^{-4} \cdot C_{\text{cf}}(B - V) \cdot S_{\text{phot}}. \quad (5)$$

So, combining this with Eq. 3, we get:

$$R'_{\text{HK}} = 1.34 \cdot 10^{-4} \cdot C_{\text{cf}}(B - V) \cdot (S - S_{\text{phot}}). \quad (6)$$

We measured the S_{phot} using Eq. 1 again. Following Hartmann et al. (1984), we subtract the core emission line from the H & K passbands in the spectrum where we

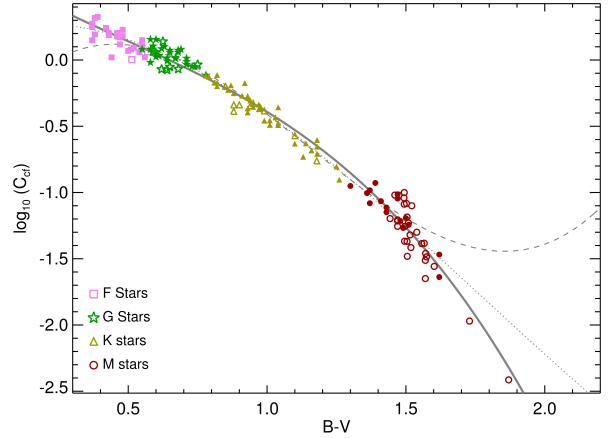


Figure 2. Conversion factor C_{cf} against $B - V$ colour for the combination of our sample stars (empty symbols) and the Rutten (1984) sample (filled symbols). The curves are third-order least-squares polynomial fits. The solid line represents our relation, the dotted line represents the Rutten (1984) relation and the dashed lines represents the Middelkoop (1982) relation.

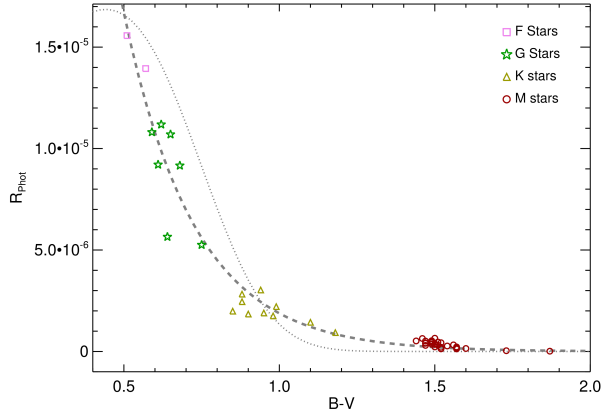


Figure 3. Measured R_{phot} against the colour of our sample stars. The grey dashed line shows the best fit to the data. The grey dotted line shows the original calibration by Hartmann et al. (1984). Differences between these curves could be due to a slightly different behaviour of the instruments on which they are based.

recorded the lowest activity, measure the residual flux inside the bands and then compute the index. To do that we defined the limits of the core emission line inside the filter, as a 0.7 \AA rectangular window around the core-emission lines for F-G-K stars and a 0.4 \AA window for M-dwarfs, and measured the flux outside those limits. The best fit to the data is given by the following equation, but we note that a larger stellar sample would be convenient to establish a proper calibration:

$$\log_{10}(R_{\text{phot}}) = 1.48 \cdot 10^{-4} \cdot \exp[-4.3658 \cdot (B - V)] \quad (7)$$

The quantity we are finally using to compare the chromospheric activity level of different stars is $\log_{10}(R'_{\text{HK}})$. Using our direct measurements for each of the quantities involved in the definition of the index ensures the validity of

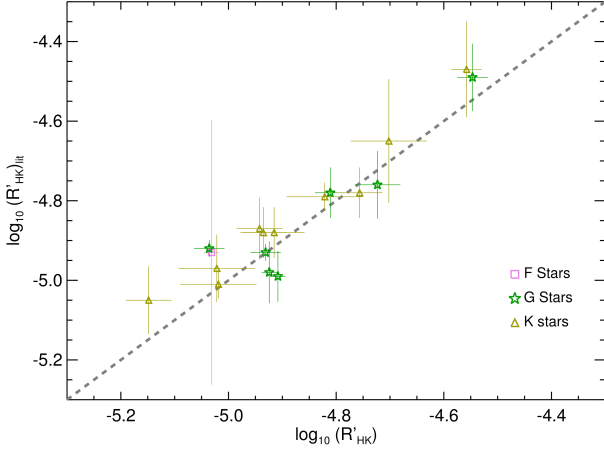


Figure 4. Comparison between the $\log_{10}(R'_{\text{HK}})$ values found in the literature and our measured $\log_{10}(R'_{\text{HK}})$. The dashed grey line represents the 1:1 line.

Table 1. $\log_{10}(R'_{\text{HK}})$ comparison data

Star	Sp. Type	$\log_{10}(R'_{\text{HK}})_{\text{Lit}}$	$\log_{10}(R'_{\text{HK}})$	Ref.
HD30495	G2	-4.49 ± 0.12	-4.52 ± 0.03	2,4
HD224789	K1	-4.47 ± 0.17	-4.55 ± 0.03	1,2
Corot-7	K3	-4.65 ± 0.22	-4.70 ± 0.07	3
HD63765	G9	-4.76 ± 0.12	-4.77 ± 0.04	1,2,5
HD104067	K3	-4.78 ± 0.09	-4.77 ± 0.04	2,5
HD1320	G2	-4.78 ± 0.09	-4.79 ± 0.03	2
HD125595	K4	-4.79 ± 0.05	-4.82 ± 0.07	5
HD134060	G2	-4.98 ± 0.11	-4.89 ± 0.01	1,2
HD1388	G2	-4.99 ± 0.09	-4.89 ± 0.01	1,2
HD2071	G2	-4.93 ± 0.03	-4.89 ± 0.03	1,2
HD176986	K3	-4.88 ± 0.09	-4.90 ± 0.04	1,2
HD41248	G2	-4.92 ± 0.03	-4.90 ± 0.03	6
HD215152	K2	-4.88 ± 0.09	-4.92 ± 0.06	1,2
HD4628	K2	-4.87 ± 0.11	-4.94 ± 0.04	2,4
HD40307	K2	-5.01 ± 0.05	-5.02 ± 0.07	1,2
HD85512	K6	-4.97 ± 0.12	-5.02 ± 0.07	1,2,7
HD1581	F9	-4.93 ± 0.47	-5.03 ± 0.01	1,2
HD77338	K2	-5.05 ± 0.12	-5.11 ± 0.04	2

Literature values are the mean of the values reported in different sources and the error bars are the standard deviations of the different measurements for a given star. Uncertainties in our reported values are the standard deviation of the individual measurements.

References: 1 - Lovis et al. (2011), 2 - Pace (2013), 3 - Queloz et al. (2009), 4 - Noyes et al. (1984), 5 - Ségransan et al. (2011), 6 - Jenkins et al. (2013), 7 - Pepe et al. (2011)

the index for the full spectral range of our sample. Our new calibration provides an extension of the $\log_{10}(R'_{\text{HK}})$ index beyond the spectral range for which it was originally designed.

Figure 4 and Table 1 shows how our $\log_{10}(R'_{\text{HK}})$ values compare to previous measurements in the literature for several stars in our sample. Table 5 lists the S , S_{phot} and $S_R + S_V$ values for each star.

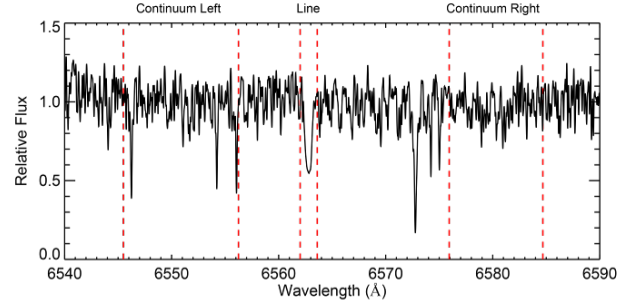


Figure 5. Spectrum of the M-type star GJ176 showing the $H\alpha$ filter passband and continuum bands.

3.2 The HARPS $H\alpha$ index

In the case of the $H\alpha$ index we use a simpler passband following Gomes da Silva et al. (2011). It consists of a rectangular bandpass with a width of 1.6 \AA and centred at 6562.808 \AA (core), and two continuum bands of 10.75 \AA and a 8.75 \AA wide centred at 6550.87 \AA (L) and 6580.31 \AA (R), respectively, as seen in Figure 5.

Thus, the $H\alpha$ index is defined as

$$H\alpha_{\text{Index}} = \frac{H\alpha_{\text{core}}}{H\alpha_L + H\alpha_R}. \quad (8)$$

4 TIME-SERIES ANALYSIS OF ACTIVITY INDICATORS AND ROTATION PERIODS

We perform a time-series analysis of the Ca II H&K and $H\alpha$ activity indicators to search for periodicities related to stellar rotation. For many stars our spectroscopic time series show that the variability of the S- and the $H\alpha$ indexes is beyond what can be explained by the error bars of the measurements. We therefore decided to search for any periodic behaviour in the series of data. We computed power spectra by fitting a sinusoidal model for each trial frequency using the MPFIT routine (Markwardt 2009) and then build a Lomb–Scargle periodogram (Lomb 1976; Scargle 1982), following Cumming (2004) and taking into account the individual error bars for each point, which makes it equivalent to the Generalised Lomb–Scargle Periodogram (Zechmeister & Kürster 2009).

To evaluate the false alarm probability of any peak in the periodogram, we follow Cumming (2004), who modified the work by Horne & Baliunas (1986) to obtain the spectral density thresholds for a desired false alarm level. This means our false alarm probability is defined as $FAP = 1 - [1 - P(z > z_0)]^M$ where $P(z > z_0) = \exp(-z_0)$ is the probability of z being greater than z_0 , with z the target spectral density, z_0 the measured spectral density and M the number of independent frequencies. We search for the power values corresponding to 31.7%, 4.6% and 0.3% false alarm probability, equivalent to 1σ , 2σ and 3σ detections. After building the power spectrum, we use the best frequency found as an initial estimate for a new sinusoidal fit of the time series.

We have not taken into account either very fast rotators or the long-term magnetic cycles of the stars. The study of these very short and very long period modulations is beyond

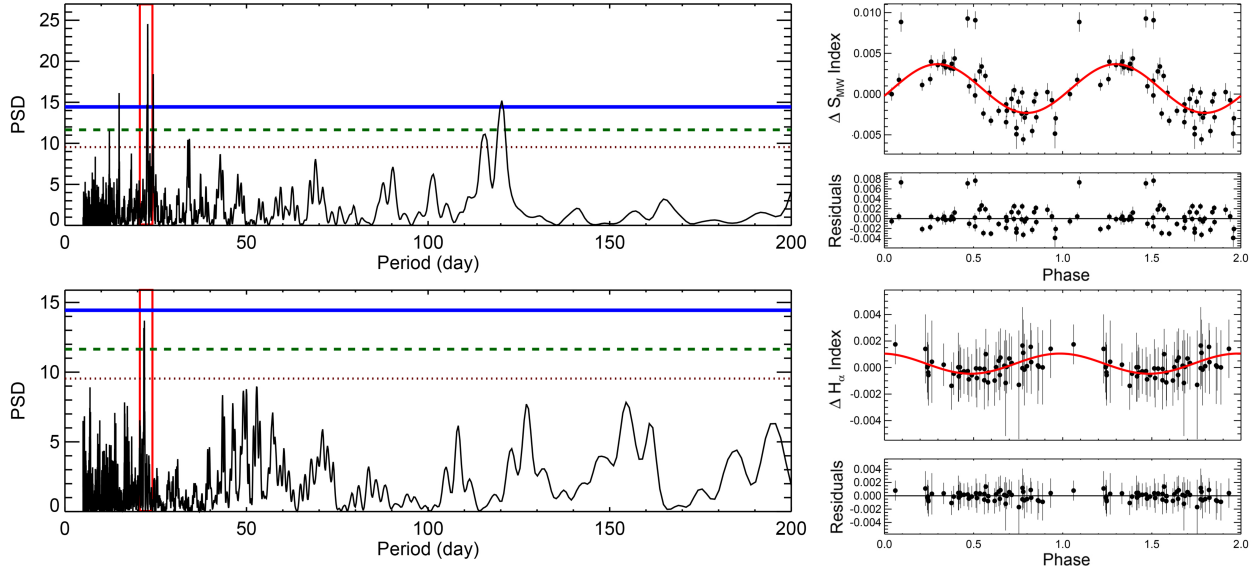


Figure 9. S_{MW} (top) and $H\alpha$ (bottom) index power spectrum and fit for the solar type star HD2071. Red dotted line represents the 1σ detection threshold, green dashed line the 2σ threshold and blue solid line the 3σ detection threshold.

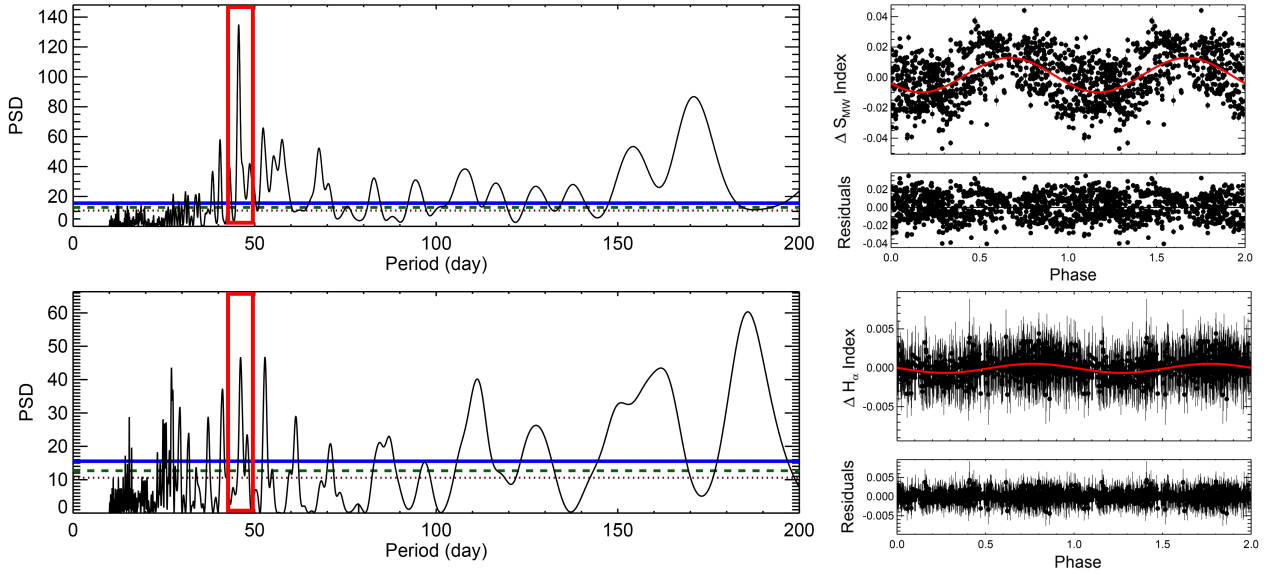


Figure 10. S_{MW} (top) and $H\alpha$ (bottom) index power spectrum and fit for the K-type star HD85512. Red dotted line represents the 1σ detection threshold, green dashed line the 2σ threshold and blue solid line the 3σ detection threshold.

the scope of this paper. Thus, the typical rotation periods we search for range from 5 to 200 days. These limits were defined after studying the typical rotation period of late type low activity main sequence stars. To cope with the presence of long term cycles we proceed to fit them and remove them before performing the search for periodicities.

To illustrate the procedure, we display in Figs 6, 7 & 8 the results for the M3 dwarf star GJ176, for which a rotational period of 38.92 ± 3.9 days has been claimed by

(Kiraga & Stepień 2007), and for which an in-depth study has been carried out by Robertson et al. (2015). Our spectroscopic periods obtained from Ca II H&K and $H\alpha$ are consistent to within 0.1 days, and the average value is 39.3 days (see Table 3), which is more precise and in good agreement with the previous value.

In the example of GJ176 the detection of the rotation period is straightforward (see Fig. 7). Both indexes give the same result and the periodogram is clear. But that is not

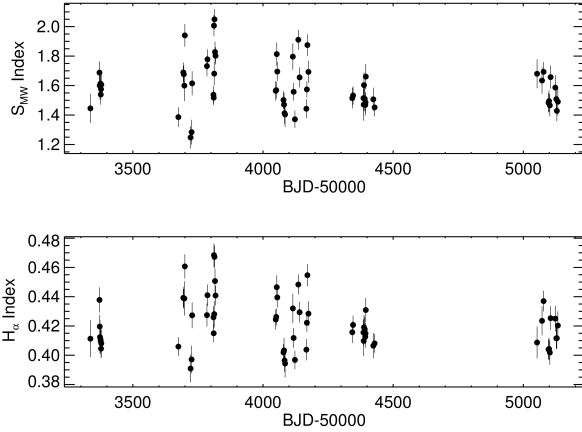


Figure 6. S_{MW} (top) and $H\alpha$ (bottom) index time series for the star GJ176.

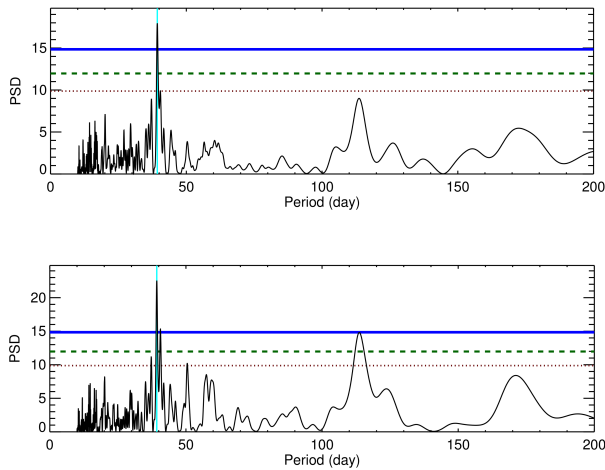


Figure 7. S_{MW} (top) and $H\alpha$ (bottom) index power spectrum showing a peak at ~ 39.3 days for GJ176. Red dotted line represents the 1σ detection threshold, green dashed line the 2σ threshold and blue solid line the 3σ detection threshold.

always the case. In a few cases the two indicators do not provide such a good agreement. Typically this happens when we have a weak detection in one of the indicators (in $H\alpha$ in early type stars, Ca II H&K in some late Ms). As the determined period is a weighted average between the measurements of both indicators, using the false alarm probability as weight, the strong detection becomes dominant for these stars. Sometimes multiple peaks are present because of inappropriate sampling and one could be in the situation that one of the indexes shows a harmonic of the rotation period with a stronger spectral density than the actual rotation period (Boisse et al. 2011). In such circumstances we rely in the cleanest periodogram as a starting point for the analysis. Figure 9 and 10 illustrate cases where the determination of the rotation period is not straightforward, one for a solar type star, another one for a K-type star.

Figure 9 shows the analysis of the solar type star HD2071 after correcting for a long term magnetic cycle. Ca

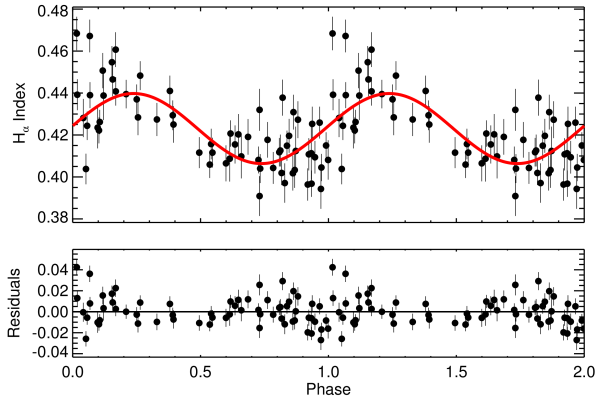
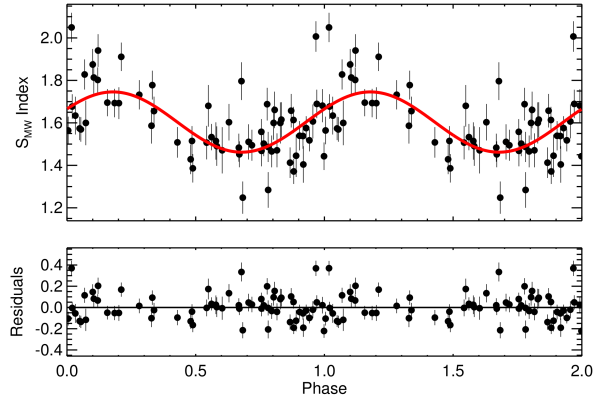


Figure 8. Fit of the S_{MW} (top) and $H\alpha$ (bottom) index data using the 39.3 days period given by the power spectrum for the star GJ176.

II H&K gives us a significant detection at ~ 22 days with a good fit to the data. Then the $H\alpha$ index, despite the low amplitude of the curve, gives us mostly the same peak. Significance is lower because of the low amplitude, but still around 1% of false alarm probability. Having both results we can conclude a rotation period for this star of 22.8 ± 0.7 days.

Figure 10 shows the analysis of the K-type star HD85512 after correcting for a long term cycle. In this situation we have a clear detection in the Ca II H&K index and a good fit to the data for a period of ~ 45 days. In the $H\alpha$ index the detection is not as clear, we have several peaks because of the low amplitude of the signal and window effects. The ~ 180 days peak is a window effect. Then we have three strong peaks at ~ 25 , ~ 46 and ~ 52 days respectively, being the ~ 46 days the strongest and more consistent with the peak in the Ca II H&K index. Then the we weighted average the two measurements and obtain 45.9 ± 0.4 days as our best measurement.

In Table 3 labels explaining the different cases are given when needed.

Table 2. Parameters for equation 9

Dataset	a	b
Full	-0.808 ± 0.012	-2.536 ± 0.009
M-type Stars	-0.753 ± 0.056	-2.219 ± 0.389
$-0.5 < [\text{Fe}/\text{H}] < -0.1$	-0.821 ± 0.025	-2.610 ± 0.066
Solar $[\text{Fe}/\text{H}]$	-0.773 ± 0.017	-2.347 ± 0.002
$+0.1 < [\text{Fe}/\text{H}] < +0.3$	-1.063 ± 0.147	-3.817 ± 0.640

4.1 Rotation Periods

Table 3 provides the rotation periods for the stars for which we have been able to detect a periodic signal. Final periods were measured by averaging the detections in the Ca_{HK} and $\text{H}\alpha$ indexes, weighting each one with the spectral density of the peaks in the corresponding periodograms. The listed uncertainties were adopted conservatively, as the difference between the periods obtained from the two indexes detections. Fig. 11 depicts the agreement between the periods derived from the Ca_{HK} and $\text{H}\alpha$.

Figure 14 and Table 3 show how our detections compare with previous determinations of the rotation periods of stars in our sample. There is, in general, very good agreement.

Figure 12 depicts the relation between our spectroscopic periods and the mean activity level measured using the Ca II H&K lines, $\log_{10}(R'_{\text{HK}})$. The two quantities show an evident correlation that is described well by the following linear fit:

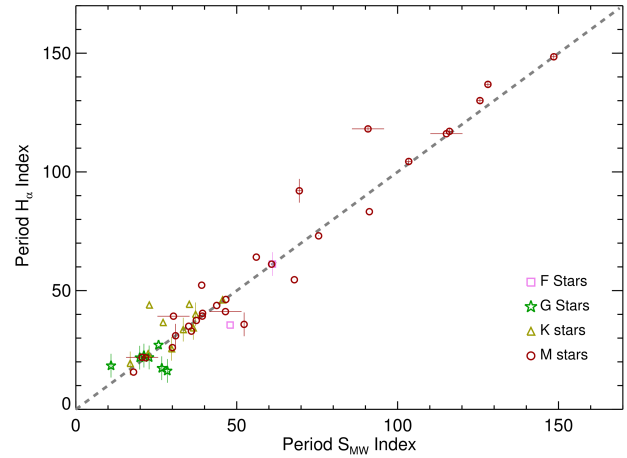
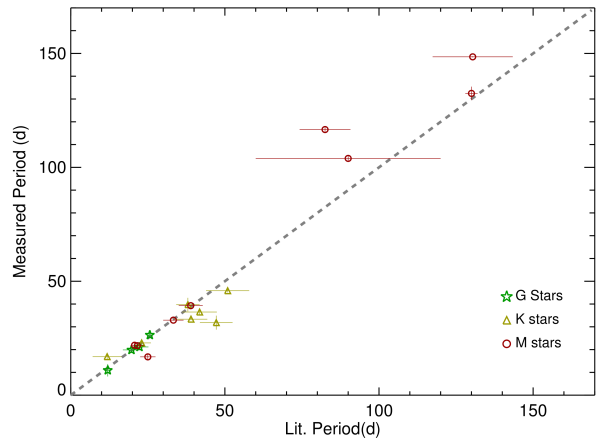
$$\log_{10}(P) = a \cdot \log_{10}(R'_{\text{HK}}) + b, \quad (9)$$

with values for the parameters a and b as given in Table 2, being the scatter of the residuals after the fit smaller than the 17% of the measured periods.

This relationship appears to be very reliable for M-type dwarfs, which populate the full range of stellar activity and rotation periods in the sample. We think this relation could be used to estimate the rotation periods of M-dwarfs from the more simple measurement of the activity level. While F-, G-, and K-type stars also lie on the relation, the lack of stars of these types at very low activity level ($\log_{10}(R'_{\text{HK}})$ below -5) leads us to recommend caution when estimating rotation periods of early-type stars via this relationship.

In principle metallicity may have an effect on the scatter seen in Figure 12. In order to establish whether or not this is the case, we studied the rotation period–chromospheric level relation for three different metallicity ranges. In Fig. 13 we display this relation for stars binned in each of these metallicity ranges. The plots show the absence of any clear dependence in the relatively small metallicity range of our stars. The metallicities used can be seen in Table 5 and have been taken from Sousa et al. (2008), Santos et al. (2013), Tsantaki et al. (2013), Ramírez, Allende Prieto & Lambert (2013) and Neves et al. (2014).

The Ca II H&K and $\text{H}\alpha$ lines have proved to be good indicators in the search for rotational modulation. Other lines could also correlate well with rotation. As shown by Gomes da Silva et al. (2011) and Robertson et al. (2015), the Na I line, which should be included in future studies, also appears to be efficient at detecting stellar rotation periods.


Figure 11. Comparison of the spectroscopic periods measured from the Ca_{HK} and $\text{H}\alpha$ indexes. The line shows the 1:1 relation.

Figure 14. Proposed spectroscopic periods versus previous period determinations available in the literature. Only a handful of stars in the sample have previous determinations. The line shows the 1:1 relation.

5 IMPLICATIONS FOR PLANET-HOSTING CANDIDATES

Previous studies of rotational modulation have questioned the existence of some planets through the use of periodograms of time-series measurements of activity indicators (e.g. Robertson et al. 2014). We have examined the orbital periods of exoplanet claims for our sample of stars in the light of the rotational periods that we have measured and found periodic signals in the activity time-series of several stars that are very similar to the orbital periods of planet candidates previously reported in the literature. We comment below on these, stars which are also listed in Table 4:

GJ 581: this star hosts a multi-planetary system, the real existence of some of the planets being questioned from the analysis of chromospheric activity time series. It was originally claimed to have 6 planets: planet b at $\sim 5.4d$ (Bonfils et al. 2005), planet c at $\sim 12.9d$ and d at $\sim 66.6d$ (Udry et al. 2007), planet e at $\sim 3.1d$ (Mayor et al. 2009a),

Table 3. Rotational Periods and Chromospheric Activity

Name	SpTp	B-V	$\log_{10}(R'_{\text{HK}})^a$	Period (d) ^b	Sig. ^c	Lit. Period (d)	Reference	Comments
HD30495	G2	0.64	-4.52 ± 0.03	10.9 ± 5.3	3σ	12.0 ± 1.2^d	Wright et al. (2004)	1,3
HD224789	K1	0.88	-4.55 ± 0.03	16.9 ± 1.8	3σ	11.8 ± 4.7	Lovis et al. (2011)	3
GJ358	M2	1.52	-4.69 ± 0.10	16.8 ± 1.6	2σ	25.0 ± 2.5^d	Kiraga & Stepien (2007)	
Corot-7	K0	0.85	-4.70 ± 0.07	22.9 ± 0.7	3σ	23.0 ± 3.0	Léger et al. (2009)	1
HD63765	G5	0.75	-4.77 ± 0.04	26.7 ± 6.7	3σ			4
HD104067	K3	0.98	-4.77 ± 0.04	29.8 ± 3.1	3σ			3
HD1320	G2	0.65	-4.79 ± 0.03	28.4 ± 8.7	2σ			1,3
GJ382	M1	1.48	-4.80 ± 0.06	21.7 ± 0.1	3σ	21.6 ± 2.2	Kiraga & Stepien (2007)	
HD125595	K4	1.10	-4.82 ± 0.07	37.2 ± 2.0	3σ			1,3
GJ846	M1	1.47	-4.84 ± 0.04	31.0 ± 0.1	3σ			
HD134060	G1	0.62	-4.89 ± 0.01	21.2 ± 1.1	3σ	22.3 ± 2.9	Lovis et al. (2011)	1
HD1388	G0	0.59	-4.89 ± 0.01	19.9 ± 1.4	3σ	19.7 ± 2.8	Lovis et al. (2011)	1,3
HD2071	G2	0.68	-4.89 ± 0.03	22.8 ± 0.7	3σ			1,3
HD41248	G1	0.61	-4.90 ± 0.03	26.4 ± 1.1	3σ	25.65 ± 1.13	Santos et al. (2014)	
HD176986	K3	0.94	-4.90 ± 0.04	33.4 ± 0.2	3σ	39.0 ± 5.3	Lovis et al. (2011)	3
Sun	G2		-4.91			26.09		
GJ3470	M2	1.50	-4.91 ± 0.11	21.9 ± 1.0	3σ	20.7 ± 0.15	Biddle et al. (2014)	1,2
HD215152	K3	0.99	-4.92 ± 0.06	36.5 ± 1.6	3σ	41.8 ± 5.6	Lovis et al. (2011)	1,3
HD25171	F9	0.51	-4.92 ± 0.17	35.6 ± 8.9	2σ			3
HD4628	K2	0.90	-4.94 ± 0.04	39.7 ± 6.4	2σ	38.0 ± 3.8^d	Noyes et al. (1984)	1,4
GJ205	M1	1.47	-4.96 ± 0.06	35.0 ± 0.1	3σ			
GJ676A	M0	1.44	-4.96 ± 0.04	41.2 ± 3.8	3σ			2
GJ176	M3	1.54	-4.99 ± 0.07	39.3 ± 0.1	3σ	38.92 ± 3.9^d	Kiraga & Stepien (2007)	
HD40307	K3	0.95	-5.02 ± 0.07	31.8 ± 6.7	3σ	47.2 ± 5.3	Lovis et al. (2011)	4
HD85512	K6	1.18	-5.02 ± 0.07	45.9 ± 0.4	3σ	50.9 ± 7.0	Lovis et al. (2011)	1
HD1581	F9	0.57	-5.03 ± 0.01	31.1 ± 0.1	2σ			3
GJ674	M3	1.57	-5.07 ± 0.08	32.9 ± 0.1	3σ	33.29 ± 3.3^d	Kiraga & Stepien (2007)	
GJ514	M1	1.48	-5.10 ± 0.06	28.0 ± 2.9	3σ			
HD77338	K2	0.88	-5.11 ± 0.04	33.4 ± 10.0	3σ			1,4
GJ849	M2	1.50	-5.14 ± 0.04	39.2 ± 6.3	3σ			2
GJ752A	M2	1.52	-5.16 ± 0.07	46.5 ± 0.3	3σ			
GJ880	M2	1.51	-5.18 ± 0.07	37.5 ± 0.1	3σ			1
GJ832	M2	1.50	-5.21 ± 0.07	45.7 ± 9.3	3σ			1,4
GJ536	M1	1.47	-5.22 ± 0.07	43.8 ± 0.1	3σ			1
GJ526	M1	1.49	-5.31 ± 0.07	52.3 ± 1.7	3σ			3
GJ436	M1	1.47	-5.32 ± 0.07	39.9 ± 0.8	3σ			
GJ588	M2	1.50	-5.34 ± 0.10	61.3 ± 6.5	3σ			1
GJ1	M0	1.46	-5.35 ± 0.08	60.1 ± 5.7	3σ			
GJ163	M1	1.48	-5.37 ± 0.11	61.0 ± 0.3	3σ			
GJ357	M3	1.57	-5.38 ± 0.13	74.3 ± 1.7	3σ			
GJ876	M3	1.56	-5.42 ± 0.07	87.3 ± 5.7	3σ	95.0 ± 1.0	Nelson et al. (2015)	
GJ433	M2	1.51	-5.50 ± 0.06	73.2 ± 16.0	3σ			4
GJ273	M3	1.57	-5.52 ± 0.07	115.6 ± 19.4	3σ			2
GJ667C	M3	1.57	-5.62 ± 0.08	103.9 ± 0.7	3σ	90.0 ± 30.0	Robertson & Mahadevan (2014)	
GJ551	M6	1.87	-5.65 ± 0.17	116.6 ± 0.7	3σ	82.5 ± 8.25^d	Kiraga & Stepien (2007)	
GJ701	M2	1.52	-5.65 ± 0.04	127.8 ± 3.2	3σ			1
GJ877	M2	1.50	-5.72 ± 0.06	116.1 ± 0.7	3σ			2
GJ581	M4	1.60	-5.79 ± 0.03	132.5 ± 6.3	3σ	130 ± 2.0	Robertson et al. (2014)	
GJ699	M5	1.73	-5.86 ± 0.11	148.6 ± 0.1	3σ	130.4 ± 13.0^d	Benedict et al. (1998)	1

^aError bars in the $\log_{10}(R'_{\text{HK}})$ come from the standard deviation of individual measurements. ^bPeriod stands for the spectroscopic determination of rotation period in days. Uncertainties are inferred from the difference measured Ca_{HK} and $\text{H}\alpha$ indicators.

^cSignificance. Related to the false alarm probability of period detections with 3σ equivalent to or less than 0.3%.

^dFor this period available in the literature, no uncertainty is provided, and thus 10% of measured period is adopted.

Notes: Kiraga & Stepien (2007), Léger et al. (2009), Biddle et al. (2014), Benedict et al. (1998) and Biddle et al. (2014) periods are derived using photometric time series. Noyes et al. (1984) derives the periods using an activity–rotation model. Lovis et al. (2011) periods are derived using Mamajek & Hillenbrand (2008) activity–rotation model. Wright et al. (2004) uses Noyes et al. (1984) procedure. Santos et al. (2014) uses activity diagnosis analysis on the radial velocity time series. Robertson & Mahadevan (2014) uses Engle & Guinan (2011) relation based on X-ray emission. Nelson et al. (2015) uses $H\alpha$ time-series analysis. Sun values taken from Donahue, Saar & Baliunas (1996); Mamajek & Hillenbrand (2008).

Comments: 1 - Presence of a long term magnetic cycle. 2 - Weak Ca_{HK} detection. 3 - Weak $\text{H}\alpha$ detection. 4 - Two different detections.

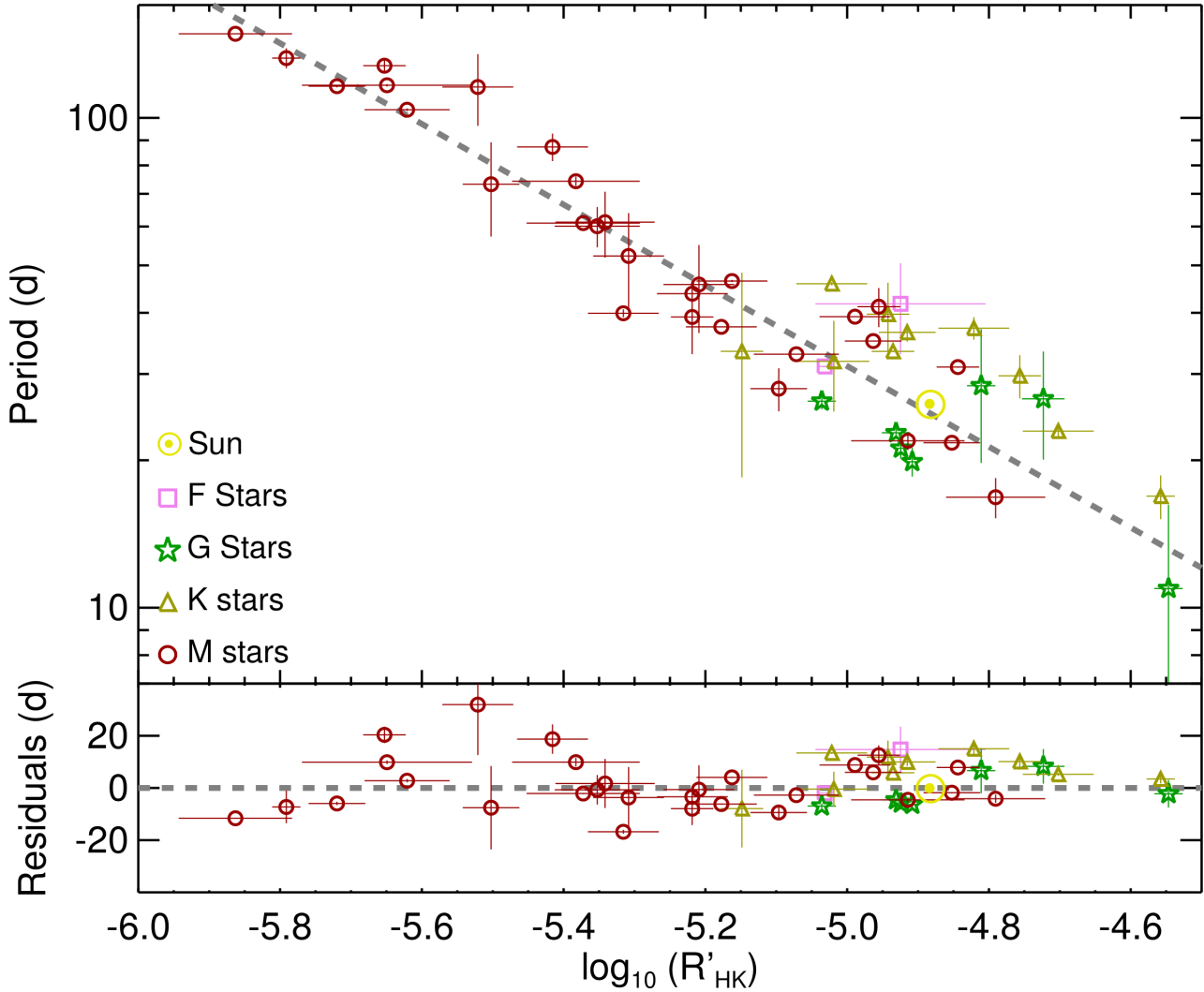


Figure 12. Rotation period versus chromospheric activity level $\log_{10}(R'_{\text{HK}})$. The dashed line shows the global fit to the full dataset. Error bars in rotation periods reflect differences in the period measurements obtained from the two activity indexes. Error bars in the $\log_{10}(R'_{\text{HK}})$ come from the standard deviation of individual measurements. For the Sun we adopted the rotation period of 26.09 days (Donahue, Saar & Baliunas 1996) and a $\log_{10}(R'_{\text{HK}})$ of -4.906 (Mamajek & Hillenbrand 2008)

and planets f $\sim 436d$ and g at $\sim 36d$ (Vogt et al. 2010). Planets d and g have been challenged as artefacts of stellar rotation (Robertson et al. 2014). Our own analysis of time series using HARPS spectra gives a rotation period of $\sim 132d$ for this star. This is about twice and 4 times the orbital periods of planet d and g, respectively (see Table 4). Boisse et al. (2011) explains the possible origin of this kind of signals as an effect of the latitude of the stellar structures and the line of sight. Our independent measurement of rotation period adds support to the conclusion of Robertson et al. (2014).

GJ 667C: this is a 5-planet candidate system: planets b at $\sim 7.2d$ and c at $\sim 28.1d$ (Bonfils et al. 2013), and planets d at $\sim 91.6d$, e at $\sim 62.2d$ and f at $\sim 39.0d$ (Gregory 2012; Anglada-Escudé et al. 2013). Recently, Robertson & Mahadevan (2014) and Feroz & Hobson (2014) claimed that

planets d and e are artefacts induced by stellar rotation. Delfosse et al. (2013) had already identified the $91d$ signal as an alias of an $\sim 106d$ activity signal. Planet d, at $91d$, is relatively close to our rotational period of $103d$, but we also found a power excess at $\sim 91d$ in the S_{MW} periodogram, supporting the idea that the signal is in fact an alias of the stellar rotation. For planet e, the claimed $62d$ orbital period is very close to $P_{\text{rot}} \cdot 2/3$ (Santos et al. 2014), casting doubts on its existence.

GJ 676A: this star has 4 detected planets: planet b at $\sim 1050d$ (Forveille et al. 2011), planet c at $\sim 4400d$, planet d at $\sim 3.6d$ and planet e at $\sim 35.4d$ (Anglada-Escudé & Tuomi 2012). The latter, planet e, has an orbital period compatible with our measured stellar rotation period ($41.2d$). This makes us suspect that it could be an activity-induced signal and not a real planet.

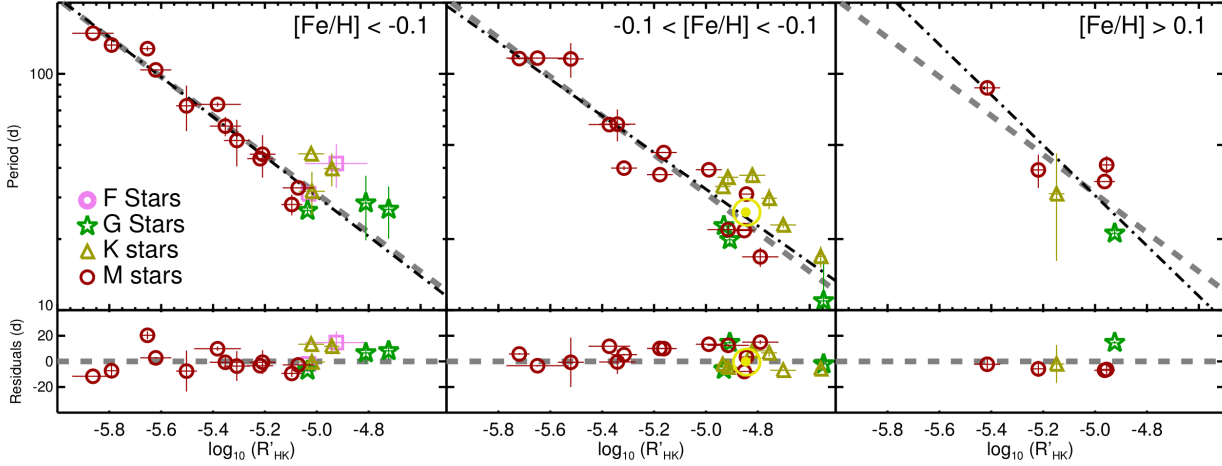


Figure 13. Rotation periods versus chromospheric activity level $\log_{10}(R'_{\text{HK}})$ in three metallicity intervals. The grey dashed line shows the fit to the full dataset, while the black dashed lines show individual fits for each metallicity subset.

GJ 832: there are 2 potential planets: planet b at $\sim 3416d$ (Bailey et al. 2009) and planet c at $\sim 35.7d$ (Wittenmyer et al. 2014). The latter has an orbital period that falls inside the error bar of our value of stellar rotation period of $45.7d$, being really close to the Ca II H&K period measurement. Bonfils et al. (2013) also found the signal of planet c, but noticed a power excess at ~ 40 days in the bi-sector periodogram. Further investigation is needed in order to confirm or reject the existence of planet c.

HD 40307: After Mayor et al. (2009b) initial claim of 3 super-Earths at 40.3, 9.6 and 20.4d, Tuomi et al. (2013) expanded the system to six planets, planet e being a small super-Earth at ~ 34.6 day orbital period. This period coincides within the uncertainties with our stellar rotation detection ($31.8d$) and therefore the existence of the planet is in question.

HD 41248: Jenkins et al. (2013) claimed the detection of two super-Earths, at periods ~ 18 and ~ 25 days. However, Santos et al. (2014) attributed these signals to the rotation period of the star at ~ 25 d and to differential rotation (~ 18 days) across different latitudes. Our analysis of time series of activity indicators confirm the stellar rotation period of ~ 25 d and therefore adds support to the doubts raised concerning the existence of at least one of these planets.

6 CONCLUSIONS

Using more than 6400 high resolution spectra from the HARPS public database we have analysed the time variability of the Ca II H&K and H α lines in a sample of 48 late-type main sequence stars, of which 29 are M-dwarfs.

We have been able to derive consistent periodicities in the time series of these activity indicators for relatively quiet stars ($\log_{10}(R'_{\text{HK}}) < -4.5$) of spectral types late F to mid M. From these periodic signals we infer stellar rotation periods for the full sample of 48 stars. The derived periods cover the range 10–150 d. The average uncertainty of our period

determinations is less than $\sim 10\%$ of the measured period, being $\sim 5\%$ the median value of the error distribution. The rotation periods inferred from the Ca II H & K and the H α indexes are consistent within these uncertainties and compatible with periods inferred from photometric modulations reported in the literature.

We have investigated the correlation between the chromospheric emission, represented by the $\log_{10}(R'_{\text{HK}})$ index, and the derived spectroscopic periods, and we have obtained a linear relationship between this index and the logarithm of the rotation period, which for M dwarfs is valid in the range $\log_{10}(R'_{\text{HK}}) \sim -4.5$ to ~ -5.8 , and independent of metallicity in the range $-0.3 < [\text{Fe}/\text{H}] < 0.3$. This relationship allows us to predict the rotational period of an M-dwarf star from spectroscopic time-series measurements. F-, G- and K-type stars in our sample also verify this relationship, although we have been able to explore a much limited range of chromospheric activity for these stars.

The radial velocity jitter caused by stellar chromospheric activity is a major concern in the search for terrestrial planets using RV surveys. Among other effects, the signal induced by stellar rotation could easily be mistaken for the detection of low-mass planetary signals. Some of our measured rotation periods are indeed similar to orbital periods of candidate planets reported in the literature, casting some doubts on the existence of several of these planets. New generations of spectrographs will be able to measure radial velocities with a precision of a few cm s^{-1} , and a limiting factor for the detection of a terrestrial planet will probably be the activity of the stars. We have shown that the signal induced by stellar rotation can be systematically detected using spectral signatures present in the same high-quality spectra required for terrestrial planet detection in RV surveys. Further studies are needed to characterize and disentangle stellar activity-induced signals from terrestrial planet signals in time series of high-precision RV measurements.

Table 4. Planet candidates with orbital periods close to rotation periods of stars in the sample

Star	Rot. Period [d]	Planet	Orb. Period [d]	Semi Amp. [m/s]	Ref
GJ581	132.5 ± 6.3	d	66.64 ± 0.08	2.63	1,8
		g	36.65 ± 0.52	1.5	2,8
GJ667C	103.9 ± 0.7	d	91.61 ± 0.89	1.52	3,9
		e	62.2 ± 0.55	0.92	3,9
GJ676A	41.2 ± 3.8	e	35.7 ± 0.07	2.62	4
GJ832	45.7 ± 9.3	c	35.68 ± 0.03	1.6	5
HD40307	31.8 ± 6.7	e	36.64 ± 0.20	0.85	6
HD41248	26.4 ± 1.1	b	18.36 ± 0.07	2.93	7,10
		c	25.65 ± 1.13	1.84	7,10

Ref: 1 - Udry et al. (2007), 2 - Vogt et al. (2010), 3 - Anglada-Escudé et al. (2013), 4 - Anglada-Escudé & Tuomi (2012), 5 - Wittenmyer et al. (2014), 6 - Tuomi et al. (2013) 7 - Jenkins et al. (2013) 8 - Robertson et al. (2014) 9 - Robertson & Mahadevan (2014), 10 - Santos et al. (2014)

ACKNOWLEDGEMENTS

This work has been partially financed by the Spanish Ministry project AYA2011-26244. J.I.G.H. also acknowledges the support from Spain's Ministry of Economy and Competitiveness (MINECO) under the 2011 Severo Ochoa Program MINECO SEV-2011-0187. This work is based on data obtained ARPS public database at the European Southern Observatory (ESO). This research has made extensive use of the SIMBAD database, operated at CDS, Strasbourg, France and NASAs Astrophysics Data System. We are grateful to all the observers of the following ESO projects, whose data we are using 60.A-9036, 072.C-0096, 073.C-0784, 073.D-0038, 073.D-0578, 074.C-0012, 074.C-0364, 074.D-0131, 075.D-0194, 076.C-0878, 076.D-0130, 076.C-0155, 077.C-0364, 077.C-0530, 078.C-0044, 078.C-0833, 078.D-0071, 079.C-0681, 079.C-0927, 079.D-0075, 080.D-0086, 081.C-0148, 081.D-0065, 082.C-0212, 082.C-0308, 082.C-0315, 082.C-0718, 083.C-1001, 083.D-0040, 084.C-0229, 085.C-0063, 085.C-0019, 085.C-0318, 086.C-0230, 086.C-0284, 087.C-0368, 087.C-0831, 087.C-0990, 088.C-0011, 088.C-0323, 088.C-0353, 088.C-0662, 089.C-0050, 089.C-0006, 090.C-0421, 089.C-0497, 089.C-0732, 090.C-0849, 091.C-0034, 091.C-0866, 091.C-0936, 091.D-0469, 180.C-0886, 183.C-0437, 183.C-0972, 188.C-0265, 190.C-0027, 191.C-0505, 191.C-0873, 282.C-5036.

REFERENCES

- Anglada-Escudé G., Tuomi M., 2012, *A&A*, 548, A58
 Anglada-Escudé G. et al., 2013, *A&A*, 556, A126
 Bailey J., Butler R. P., Tinney C. G., Jones H. R. A., O'Toole S., Carter B. D., Marcy G. W., 2009, *ApJ*, 690, 743
 Baliunas S. L. et al., 1983, *ApJ*, 275, 752
 Baliunas S. L., Henry G. W., Donahue R. A., Fekel F. C., Soon W. H., 1997, *AJ*, 474, L119
 Benedict G. F. et al., 1998, *AJ*, 116, 429
 Biddle L. I. et al., 2014, *MNRAS*, 443, 1810
 Boisse I., Bouchy F., Hébrard G., Bonfils X., Santos N., Vaclair S., 2011, *A&A*, 528, A4
 Bonfils X. et al., 2013, *A&A*, 549, A109
 Bonfils X. et al., 2005, *A&A*, 443, L15
 Brandt P. N., Solanki S. K., 1990, *A&A*, 231, 221
 Catalano S., Marilli E., 1983, *AAP*, 121, 190
 Cousins A. W. J., Stoy R. H., 1962, *Royal Greenwich Observatory Bulletins*, 64, 103
 Cumming A., 2004, *MNRAS*, 354, 1165
 Delfosse X. et al., 2013, *ARA&A*, 553, A8
 Donahue R. A., Saar S. H., Baliunas S. L., 1996, *ApJ*, 466, 384
 Dravins D., 1982, *ARA&A*, 20, 61
 Dravins D., 1985, in *Stellar Radial Velocities*, Philip A. G. D., Latham D. W., eds., pp. 311–320
 Dravins D., Lindegren L., Nordlund A., 1981, *A&A*, 96, 345
 Ducati J. R., 2002, *VizieR Online Data Catalog*, 2237, 0
 Dumusque X., Boisse I., Santos N. C., 2014, *ApJ*, 796, 132
 Dumusque X. et al., 2012, *Nature*, 491, 207
 Engle S. G., Guinan E. F., 2011, in *Astronomical Society of the Pacific Conference Series*, Vol. 451, 9th Pacific Rim Conference on Stellar Astrophysics, Qain S., Leung K., Zhu L., Kwok S., eds., p. 285
 Feroz F., Hobson M. P., 2014, *MNRAS*, 437, 3540
 Forveille T. et al., 2011, *A&A*, 526, A141
 Gomes da Silva J., Santos N. C., Bonfils X., Delfosse X., Forveille T., Udry S., 2011, *A&A*, 534, A30
 Gregory P. C., 2012, *ArXiv e-prints*
 Hartmann L., Soderblom D. R., Noyes R. W., Burnham N., Vaughan A. H., 1984, *ApJ*, 276, 254
 Hatzes A. P., 2013, *ApJ*, 770, 133
 Høg E. et al., 2000, *A&A*, 355, L27
 Horne J. H., Baliunas S. L., 1986, *ApJ*, 302, 757
 Howard A. W. et al., 2014, *ApJ*, 794, 51
 Huélamo N. et al., 2008, *A&A*, 489, L9
 Jao W.-C., Henry T. J., Subasavage J. P., Winters J. G., Gies D. R., Riedel A. R., Ianna P. A., 2014, *AJ*, 147, 21
 Jenkins J. S., Tuomi M., Brasser R., Ivanyuk O., Murgas F., 2013, *ApJ*, 771, 41
 Johnson H. L., 1966, *ARA&A*, 4, 193
 Kiraga M., 2012, *Acta Astron.*, 62, 67
 Kiraga M., Stepień K., 2007, *Acta Astronomica*, 57, 149
 Koen C., Killick D., van Wyk F., Marang F., 2010, *MNRAS*, 403, 1949
 Landolt A. U., 2009, *AJ*, 137, 4186
 Léger A. et al., 2009, *A&A*, 506, 287
 Lindegren L., Dravins D., 2003, *A&A*, 401, 1185
 Livingston W. C., 1982, *Nature*, 297, 208

- Lomb N. R., 1976, *AAPS*, 39, 447
- Lovis C. et al., 2011, *ArXiv e-prints*
- Lurie J. C. et al., 2014, *AJ*, 148, 91
- Mamajek E. E., Hillenbrand L. A., 2008, *ApJ*, 687, 1264
- Markwardt C. B., 2009, in *Astronomical Society of the Pacific Conference Series*, Vol. 411, *Astronomical Data Analysis Software and Systems XVIII*, Bohlender D. A., Durand D., Dowler P., eds., p. 251
- Mayor M. et al., 2009a, *A&A*, 507, 487
- Mayor M. et al., 2003, *The Messenger*, 114, 20
- Mayor M. et al., 2009b, *A&A*, 493, 639
- Mermilliod J.-C., 1986, *Catalogue of Eggen's UBV data.*, 0 (1986), 0
- Messina S., Guinan E. F., 2002, *A&A*, 393, 225
- Meunier N., Desort M., Lagrange A.-M., 2010, *A&A*, 512, A39
- Middelkoop F., 1982, *A&A*, 107, 31
- Nelson B. E., Robertson P., Payne M. J., Pritchard S. M., Deck K. M., Ford E. B., Wright J. T., Isaacson H., 2015, *ArXiv e-prints*
- Neves V., Bonfils X., Santos N. C., Delfosse X., Forveille T., Allard F., Udry S., 2014, *A&A*, 568, A121
- Noyes R. W., Hartmann L. W., Baliunas S. L., Duncan D. K., Vaughan A. H., 1984, *ApJ*, 279, 763
- Pace G., 2013, *A&A*, 551, L8
- Pepe F. et al., 2011, *A&A*, 534, A58
- Pont F., Aigrain S., Zucker S., 2011, *MNRAS*, 411, 1953
- Queloz D. et al., 2009, *A&A*, 506, 303
- Queloz D. et al., 2001, *A&A*, 379, 279
- Ramírez I., Allende Prieto C., Lambert D. L., 2013, *ApJ*, 764, 78
- Rapaport M. et al., 2001, *ARA&A*, 376, 325
- Reid I. N., Hawley S. L., Gizis J. E., 1997, *VizieR Online Data Catalog*, 3198, 0
- Robertson P., Endl M., Henry G. W., Cochran W. D., MacQueen P. J., Williamson M. H., 2015, *ArXiv e-prints*
- Robertson P., Mahadevan S., 2014, *ApJ*, 793, L24
- Robertson P., Mahadevan S., Endl M., Roy A., 2014, *Science*, 345, 440
- Rutten R. G. M., 1984, *A&A*, 130, 353
- Saar S. H., Donahue R. A., 1997, *ApJ*, 485, 319
- Santos N. C. et al., 2014, *A&A*, 566, A35
- Santos N. C. et al., 2013, *A&A*, 556, A150
- Scargle J. D., 1982, *ApJ*, 263, 835
- Ségransan D. et al., 2011, *A&A*, 535, A54
- Skumanich A., 1972, *ApJ*, 171, 565
- Sousa S. G. et al., 2008, *AAP*, 487, 373
- Tsantaki M., Sousa S. G., Adibekyan V. Z., Santos N. C., Mortier A., Israelian G., 2013, *A&A*, 555, A150
- Tuomi M., Anglada-Escudé G., Gerlach E., Jones H. R. A., Reiners A., Rivera E. J., Vogt S. S., Butler R. P., 2013, *A&A*, 549, A48
- Udry S. et al., 2007, *A&A*, 469, L43
- van Belle G. T., von Braun K., 2009, *ApJ*, 694, 1085
- van Leeuwen F., 2007, *A&A*, 474, 653
- Vaughan A. H., Preston G. W., Baliunas S. L., Hartmann L. W., Noyes R. W., Middelkoop F., Mihalas D., 1981, *ApJ*, 250, 276
- Vogt S. S., Butler R. P., Rivera E. J., Haghighipour N., Henry G. W., Williamson M. H., 2010, *ApJ*, 723, 954
- Wittenmyer R. A. et al., 2014, *ApJ*, 791, 114
- Wright J. T., Marcy G. W., Butler R. P., Vogt S. S., 2004, *ApJS*, 152, 261
- Zechmeister M., Kürster M., 2009, *A&A*, 496, 577

Table 5. Data for each star

Name	SpTp*	N.Spec	TSp*	$\langle S/N \rangle$	m_B	m_V	B-V	S	S_{phot}	$S_R + S_V$	[Fe/H]	Dist. (pc)	Ref.
HD25171	F8	30	3597	44	8.29	7.78	0.51	0.13	0.07	7.47	-0.11	55.0 ± 1.4	1, 5, 10
HD1581	F9	499	1167	125	4.80	4.23	0.57	0.15	0.09	231.62	-0.18	8.6 ± 0.1	1, 6, 11
HD1388	G0	90	1250	235	7.09	6.50	0.59	0.15	0.07	28.95	-0.01	27.2 ± 0.4	1, 6, 12
HD41248	G1	203	1843	78	9.42	8.81	0.61	0.16	0.08	2.57	-0.37	52.4 ± 1.9	1, 6, 10
HD134060	G1	110	1503	178	6.91	6.29	0.62	0.13	0.06	42.24	0.14	24.2 ± 0.3	1, 6, 10
HD30495	G2	86	864	175	6.14	5.50	0.64	0.29	0.05	53.50	0.00	13.3 ± 0.1	1, 7, 10
HD1320	G2	21	3230	135	8.63	7.98	0.65	0.22	0.09	5.77	-0.27	36.4 ± 0.9	1, 6, 12
HD176986	G2	49	3700	170	7.95	7.27	0.68	0.18	0.08	10.86	-0.09	27.2 ± 0.5	1, 6, 10
HD63765	G5	48	2302	137	8.85	8.10	0.75	0.23	0.05	5.65	-0.16	33.3 ± 0.7	1, 6, 13
Corot-7	K0	164	1437	40	12.52	11.67	0.85	0.33	0.03	0.16	0.02	150.0 ± 20.0	2, 5, 14
HD224789	K1	33	2833	113	9.12	8.24	0.88	0.54	0.05	2.46	-0.04	29.9 ± 0.6	1, 8, 10
HD77338	K1	38	3205	80	9.47	8.59	0.88	0.17	0.04	1.99	0.28	39.2 ± 1.6	1, 5, 10
HD4628	K2	164	1719	136	6.64	5.74	0.90	0.23	0.03	28.10	-0.31	7.5 ± 0.1	1, 7, 11, 15
HD176986	K3	144	3585	99	9.39	8.45	0.94	0.27	0.05	2.39	0.03	26.4 ± 0.7	1, 8, 10
HD40307	K3	442	3810	162	8.10	7.15	0.95	0.20	0.03	8.36	-0.36	13.0 ± 0.1	1, 8, 16
HD104067	K3	86	2270	142	8.90	7.92	0.98	0.33	0.03	3.95	-0.04	21.1 ± 0.4	1, 8, 16
HD215152	K3	265	3805	122	9.12	8.13	0.99	0.26	0.04	3.12	-0.08	21.5 ± 0.5	1, 8, 10
HD125595	K4	137	2075	57	10.13	9.03	1.10	0.49	0.04	1.02	0.10	28.0 ± 0.8	1, 5, 12
HD85512	K6	777	2336	128	8.83	7.65	1.18	0.45	0.04	2.63	-0.26	11.2 ± 0.1	1, 8, 16
GJ676A	M0	88	2263	44	11.03	9.59	1.44	1.40	0.06	0.29	0.26	16.5 ± 0.5	1, 9, 16
GJ1	M0	42	2063	108	10.02	8.56	1.46	0.60	0.05	1.19	-0.45	4.3 ± 0.1	1, 9, 16
GJ536	M1	104	3628	48	11.18	9.71	1.47	0.85	0.04	0.25	-0.14	10.0 ± 0.2	1, 9, 16
GJ436	M1	152	1526	33	12.06	10.59	1.47	0.65	0.05	0.12	-0.03	10.1 ± 0.3	1, 9, 10
GJ846	M1	55	2345	70	10.62	9.15	1.47	1.76	0.05	0.47	0.01	10.2 ± 0.2	1, 9, 16
GJ205	M1	76	1400	157	9.44	7.97	1.47	1.45	0.04	2.13	0.19	5.7 ± 0.1	1, 9, 16
GJ382	M1	32	1187	68	10.76	9.26	1.49	1.91	0.04	0.68	0.02	7.9 ± 0.2	1, 9, 16, 17
GJ163	M1	165	3704	26	13.30	11.81	1.49	0.55	0.04	0.07	0.07	15.0 ± 0.5	1, 9, 16
GJ526	M1	29	1790	96	9.92	8.43	1.49	0.75	0.04	1.31	-0.22	5.4 ± 0.1	1, 9, 16
GJ514	M1	114	3634	73	10.52	9.03	1.49	1.12	0.06	0.39	-0.16	7.7 ± 0.1	1, 9, 16
GJ877	M2	46	2973	43	11.87	10.38	1.50	0.33	0.05	0.16	0.00	8.6 ± 0.1	1, 9, 16
GJ849	M2	42	1893	46	11.87	10.37	1.50	0.94	0.04	0.23	0.24	8.6 ± 0.2	4, 9, 16
GJ588	M2	188	3271	55	10.81	9.31	1.50	0.85	0.04	0.32	0.06	5.9 ± 0.1	1, 9, 16
GJ832	M2	53	3134	97	10.18	8.67	1.50	0.75	0.04	0.88	-0.17	5.0 ± 0.1	1, 9, 16
GJ3470	M2	78	1434	15	13.77 [‡]	12.27	1.50	1.62	0.03	0.02	0.08	28.8 ± 2.6	3, 5, 19
GJ880	M2	77	3636	79	10.14	8.64	1.51	1.56	0.07	0.49	0.03	6.9 ± 0.1	1, 9, 16
GJ433	M2	79	2490	58	11.32	9.81	1.51	0.57	0.06	0.29	-0.17	8.9 ± 0.2	1, 9, 16
GJ752A	M2	73	3609	77	10.63	9.12	1.52	1.09	0.02	0.48	0.05	5.9 ± 0.1	1, 9, 16
GJ701	M2	68	3302	64	10.88	9.36	1.52	0.50	0.04	0.31	-0.27	7.8 ± 0.1	1, 9, 16
GJ358	M2	27	1923	47	12.21	10.69	1.52	3.03	0.04	0.19	-0.01	9.5 ± 0.2	1, 9, 16
GJ176	M3	68	2146	55	11.49	9.95	1.54	1.56	0.04	0.27	-0.01	9.3 ± 0.3	1, 9, 16
GJ876	M3	225	3089	51	11.75	10.19	1.56	0.77	0.06	0.25	0.14	4.7 ± 0.1	1, 9, 18
GJ674	M3	137	3580	81	10.97	9.41	1.57	1.56	0.04	0.56	-0.23	4.6 ± 0.1	1, 9, 16
GJ667C	M3	167	3073	48	11.79	10.22	1.57	0.60	0.03	0.20	-0.50	7.1 ± 0.2	4, 9, 12
GJ273	M3	183	2349	60	11.44	9.87	1.57	0.70	0.04	0.30	-0.01	3.8 ± 0.1	1, 9, 16
GJ357	M3	47	2521	34	12.48	10.91	1.57	0.83	0.04	0.11	-0.30	9.0 ± 0.2	1, 9, 16
GJ581	M4	251	2909	43	12.17	10.57	1.60	0.45	0.04	0.15	-0.20	6.2 ± 0.1	4, 9, 16
GJ699	M5	211	2234	54	11.24	9.51	1.73	0.68	0.03	0.23	-0.51	1.8 ± 0.1	1, 9, 16
GJ551	M6	222	3515	23	12.97	11.10	1.87	8.06	0.03	0.03	0.00	1.3 ± 0.1	4, 9, 20

References for distance: 1 - van Leeuwen (2007), 2 - Léger et al. (2009), 3 - Biddle et al. (2014), 4 - Lurie et al. (2014).

References for metallicity: 5 - Santos et al. (2013), 6 - Sousa et al. (2008), 7 - Ramírez, Allende Prieto & Lambert (2013), 8 - Tsantaki et al. (2013), 9 - Neves et al. (2014).

References for magnitudes: 10 - Høg et al. (2000)[†], 11 - Ducati (2002), 12 - Mermilliod (1986), 13 - Cousins & Stoy (1962), 14 - Léger et al. (2009) 15 - van Belle & von Braun (2009), 16 - Koen et al. (2010), 17 - Kiraga (2012), 18 - Landolt (2009), 19 - Rapaport et al. (2001), 20 - Jao et al. (2014).

* Approximate spectral type based in the colour index.

* Time span of the observations in days.

[†] Tycho magnitudes converted to Johnson magnitudes.

[‡] Not available Johnson m_B in the literature. Value calculated using the $(B - V)$ value of the star with the closest spectrum using Reid, Hawley & Gizis (1997) as guide.